Angewandte Chemie
Eine Zeitschrift der Gesellschaft Deutscher Chemiker

Supporting Information

Multimodal Imaging of Autofluorescent Sites Reveals Varied Chemical Speciation in SSZ-13 Crystals

Naomi Omori[+],* *Alessia Candeo*[+],* *Sara Mosca, Ines Lezcano-Gonzalez, Ian K. Robinson, Luxi Li, Alex G. Greenaway, Paul Collier, and Andrew M. Beale**

anie_202015016_sm_miscellaneous_information.pdf

Supplementary Material

Contents

1 Method

1.1 Sample Preparation

SSZ-13 zeolite was synthesized as described previously[1] using trimethyl adamantammonium hydroxide (Sachem Inc.) as structure-directing agent. Identity and purity of the zeolite were verified by XRD (see below).

Calcination in all cases involved placing the sample in a ceramic dish in a static oven and heating in air to 120 °C at 1 °C/min and holding at temperature for 2.5 h, then heating to the target temperature (i.e. 550 or 630 °C) at 4 °C/min and holding at the nominated temperature for 10 h.

1.2 Scanning Electron Microscopy (SEM)

SEM images were obtained on a JSM-6701F Field Emission Scanning Electron Microscope (JEOL, Tokyo) using the equipped secondary electron (SE) detector. Images were obtained under high vacuum (5.15×10^{-7} torr/6.87×10^{-5} Pa) at 10 kV with scan speed of 735. All samples were coated with gold for 35 s, but actual thickness is unknown.

1.3 Thermogravimetric Analysis (TGA)

N_2 flowed at 40 mL/min was used as a balance gas and 60 mL/min of 21% O_2 in He was used during the actual measurement. The samples were heated in air at 1 °C/minute up to 150°C and held for 2.5 hours. They were then heated to 350 °C at 2.2 °C/minute and held for 3 hours, and then heated at 0.8 °C/min to 580 °C and held for 3 hours.

1.4 X-ray Diffraction (XRD)

Powder X-ray diffraction was measured using a Rigaku Miniflex X-ray instrument with a Cu tube source of 600 mW and 1D D/teX detector and divergent slits. Diffraction patterns were collected between 5-50 2θ with an increment of 0.017 (2θ) and an acquisition time of 1 sec/step.

1.5 Confocal Fluorescence Microscopy

Confocal images were obtained on a Leica SP8 microscope (Leica Microsystems, Germany) atby exciting with a continuous wave diode laser at 405 nm (maximum power 7 mW at the sample) and with a pulsed supercontinuum laser (NKT Photonics, Denmark, maximum power 50 mW at the sample). A 63x water-immersion objective with 1.2 numerical aperture (Leica, HC Pl Apo, 63x/1.20) was used to collect images of 1024 x 1024 pixels with a field of view of 50x50 μm^2.The scanning speed of the galvanometric mirrors was set to 100 Hz, while the pinhole was opened to 1 Airy Unit at 580 nm. Notch filters at 405 nm or 488 nm were used. Single-colour images were collected using a single hybrid detector with a detection window set from 450 to 650 nm. Two-colour images were collected using two hybrid detectors at the same time, the first detection window spanning from 450 to 550 nm and the second detection window spanning from 550 to 650 nm. Z-stacks were collected with a z-step of 0.4 – 0.8 µm. Image visualisation and 3D reconstruction of the image stacks was performed in ImageJ (Fiji)[2].

1.6 Fluorescence Lifetime Imaging Microscopy (FLIM)

FLIM images were obtained on the same Leica SP8 microscope used for confocal imaging. In this case, the samples were excited only at 488 nm with a pulsed supercontinuum laser (NKT Photonics, Denmark) with repetition rate reduced to 10 MHz, which gave a timespan for the lifetime decay of almost 100 ns. The same 63x/1.2 water-immersion objective was used to collect both single plane FLIM images and 3D stacks of FLIM images of 512x512 pixels. The emission was collected from 515 nm to 700 nm. Integrated photon counting hybrid detectors were used in conjunction with a PicoHarp 300 TCSPC module (PicoQuant) (PicoQuanT GmbH, Germany). The acquisition lasted 8 minutes for single image experiments, while in 3D experiments planes were 1 µm apart and the total acquisition time was 30 minutes.

Analysis of FLIM datasets was performed with the *FLIMfit* software tool (version 5.1.1) developed by Warren et al.[3]. The images were binned twice in space and in time (4x4 spatial binning for the 3D FLIM). An experimental instrument response function (IRF) was used in the analysis. Phasor plots were generated via *FLIMfit* and used to segment the images on the basis of a common lifetime. The phasor plot method[4] provides a 2D polar plot representation of the lifetime decay histogram for each pixel, after transforming it into a phasor. A pixel-wise analysis was performed with a tri-exponential model after setting up an intensity threshold of 25 photons and a 5x5 smoothing kernel. Offset and IRF shift were left as parameters of fitting. Areas of similar lifetime were extracted with the phasor approach and then averaged and fitted. The 3D FLIM reconstructions were made with ImageJ (Fiji).

1.7 Multispectral Imaging

Multispectral imaging was performed using the λ-scan feature of the Leica SP8 microscope (Leica Microsystems, Germany) in order to extract spectral information from the confocal images. Multiple images of the same sample position were acquired with fixed excitation, while the detection band, set to 7.5 µm, was tuned by shifting the detection slit of 5 µm. Multispectral images with excitation at 405 nm were acquired from 430 nm to 690 nm, while multispectral images run at 488 nm were acquired from 500 nm to 690 nm. Spectra were extracted with the Leica SP8 LASX software by selecting regions of interest.

1.8 Raman Spectroscopy

Raman spectra were obtained from an InVia confocal Raman microscope (Renishaw, Wotton-under-Edge, UK) equipped with a 50x objective lens (Nikon, L Plan Apo, 50x/0.45, WD17) and Peltier cooled CCD. The sample was irradiated with either an 830 nm diode laser with 34 mW maximum power output, or a 514 nm Stellar PRO argon laser (Modu-laser, USA) with 10 mW maximum power output.

Attenuated laser power at the sample was achieved using neutral density filters. A grating with 1200 lines/mm was used, yielding an overall spectral resolution of 1 cm^{-1}.

Raman maps were acquired using an x-y motorised stage, which was moved in 1.5 µm steps to raster across a region of interest. At each point, Raman spectra were collected in the spectral region 1015 to 1472 cm^{-1} with an acquisition time of 20 s and 10 accumulations totalling an overall acquisition time of 18-20 hrs per map, and an irradiance of 5000 W/cm^{2}.

The spatial distribution of the most significant Raman bands were reconstructed by calculating the correlation of a triangular template (cantered at the frequency υ with a base width $\Delta\upsilon$ of 20 cm^{-1}) with the Raman spectrum detected in each analysis point in the spectral band $\Delta\upsilon$. The following method, quoted as TC descriptor[5],[6], is more selective than other mapping methods[7].

Since 830 nm was used with a long working distance objective lens, the nominal spot dimension is around 5µm and the depth of field is at least 10 µm. The entire z-depth is likely to be excited as the spectra were acquired without a pin hole, relatively high laser power, and the crystal medium's low absorption and tendency to scatter allows for greater photon propagation through the volume.

1.9 X-ray Fluorescence (XRF) Imaging

The X-ray Fluorescence (XRF) experiment was performed at the 2-ID-E microprobe hard X-ray beamline, at the Advanced Photon Source of Argonne National Laboratory, using 10keV X-ray photons, selected by a Si(111) single crystal monochromator[8]. The X-ray beam was collimated by a 500□m diameter pinhole and focused by a Fresnel Zone Plate (FZP) onto the sample. An order-sorting aperture and central stop were used to filter out the unfocused beam and higher order diffraction. The beam size was ~700nm, which defines the spatial resolution. The XRF signals were collected by a Si-drift Vortex®-ME4 energy-dispersive detector. A 30 µm SSZ-13 crystal, charged with copper using "wet ion exchange" once in Cu2+, was raster-scanned at 111 projections angles over a 330° angular range in 3° increments. The projective XRF data were processed by MAPS[9] to deconvolute single element maps. These maps were then aligned and reconstructed by MAPStoTomoPy[10] to 3D elemental distribution, using a penalized maximum likelihood algorithm in 100 iterations.

2 Additional Data

2.1 SEM

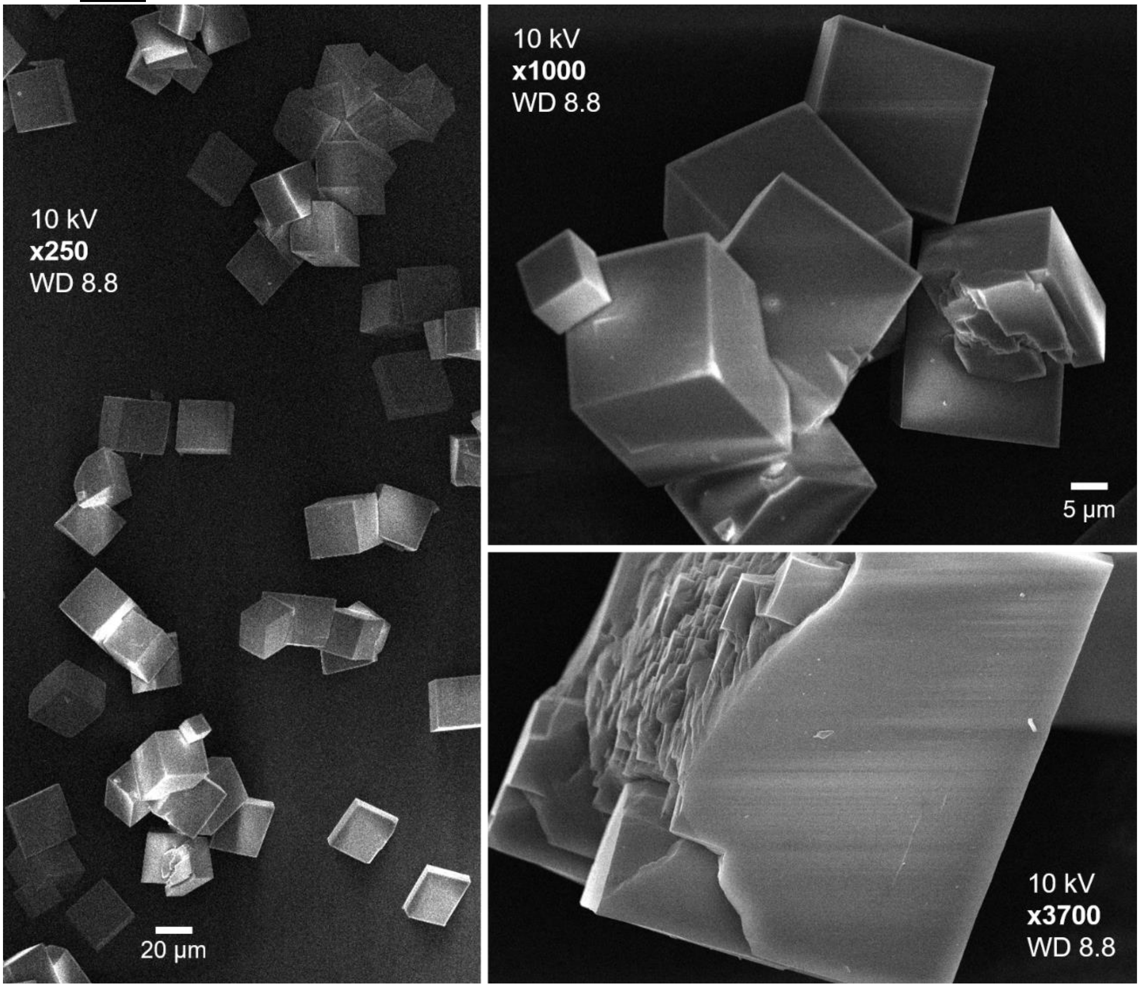

Figure S 1 ***SEM images of chabazite crystals calcined at 550°C*** *including widefield image (left), x1000 magnification cluster view and x3700 single crystal zoom (right)*

SEM images show crystals have a regular cubic crystal morphology. Some evidence of cracking is seen in specific crystals.

2.2 XRD

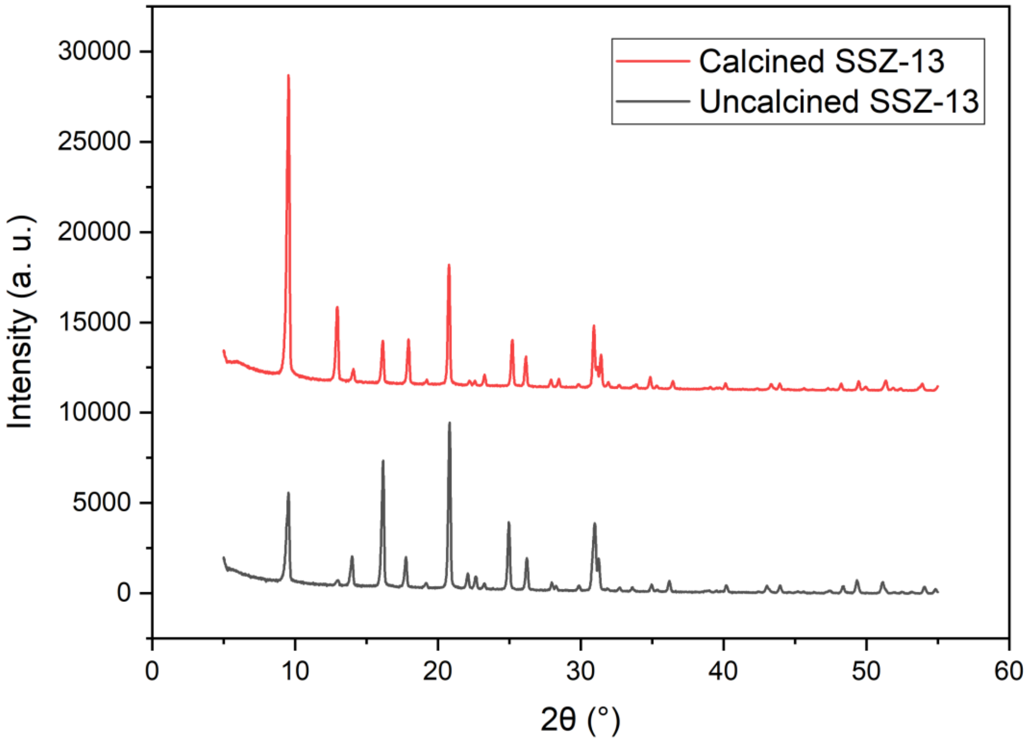

Figure S 2 ***XRD patterns for calcined (red) and uncalcined (black) SSZ-13 material***

Figure S2 shows XRD patterns for the uncalcined and calcined SSZ-13 material. The clear ensemble of peaks in both samples indicates the satisfactory crystallinity of both samples, further implying that the framework has not been adversely affected by the thermal calcination process. The position of peaks is consistent with IZA data[11].

2.3 TGA

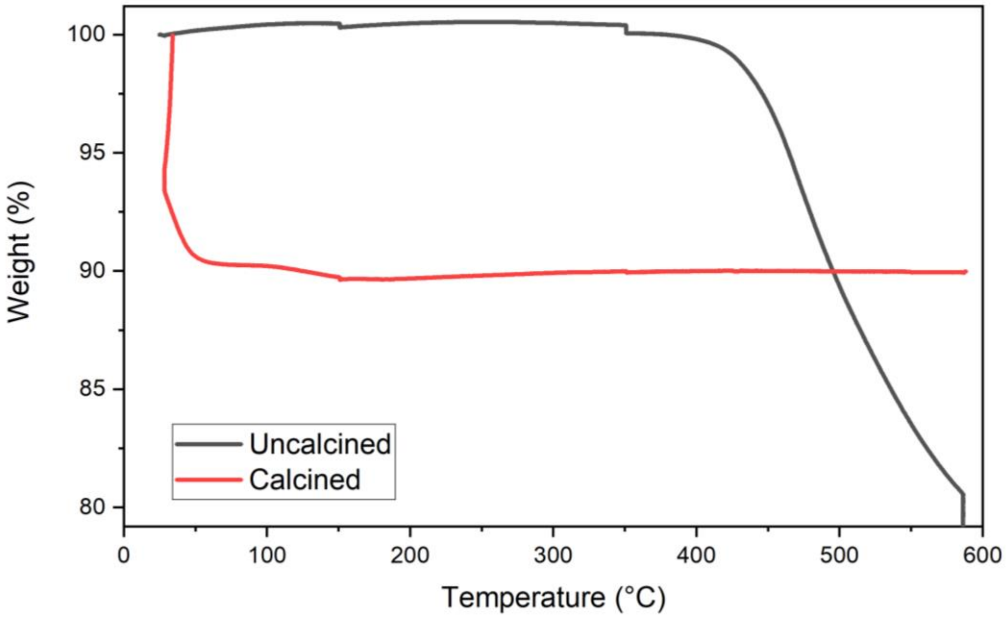

Figure S 3 ***TGA curves of uncalcined (black) and calcined SSZ-13 (red)*** *showing the percentage of the original sample weight as a function of the temperature at the sample*

Figure S3 shows TGA data for uncalcined and calcined SSZ-13 samples. Overall, the uncalcined sample loses 21% of its total mass and the calcined sample loses 10%. The uncalcined sample is known to contain organic templating agent so the higher overall mass loss is attributed to this. Below 250 °C uncalcined sample does not experience significant mass loss, indicating that both that there is little chemisorbed water due to the OSDA occupying acid sites and that the template is either broadly stable or yet to decompose sufficiently to evacuate the pores up to this temperature. A modest mass loss is visible at 150 °C during the isothermal portion of the temperature programme. The relative stability of the trace up till 300 °C may be attributed to the initial fragmentation of the template, leading to the formation of fragments that continue to be retained in the framework. Between 250 and 500 °C the largest proportion of the total mass loss is seen, and this is attributed to the removal of organics. At temperatures exceeding 500 °C and during the isothermal hold for 3 hours at 580 °C, additional mass loss is seen, implying that in template material is progressively depleted at these higher temperatures. A true detemplation would see the as-synthesised material being held at 550 °C for 10-12 hours, ensuring as much organic material is removed as practically possible.

Unlike the uncalcined SSZ-13, the calcined sample experiences the majority of its mass loss below 250 °C. The rapid mass loss below 200 °C is attributed to water loss. Beyond this temperature, the sample mass is exceedingly stable. Additionally, at 580 °C there is not any significant change in the trace. This indicates that the sample was appropriately calcined as there is no major indication of organic-related mass loss, and it indicates that the framework is thermally stable up to at least 580 °C.

2.4 Spectrofluorometer

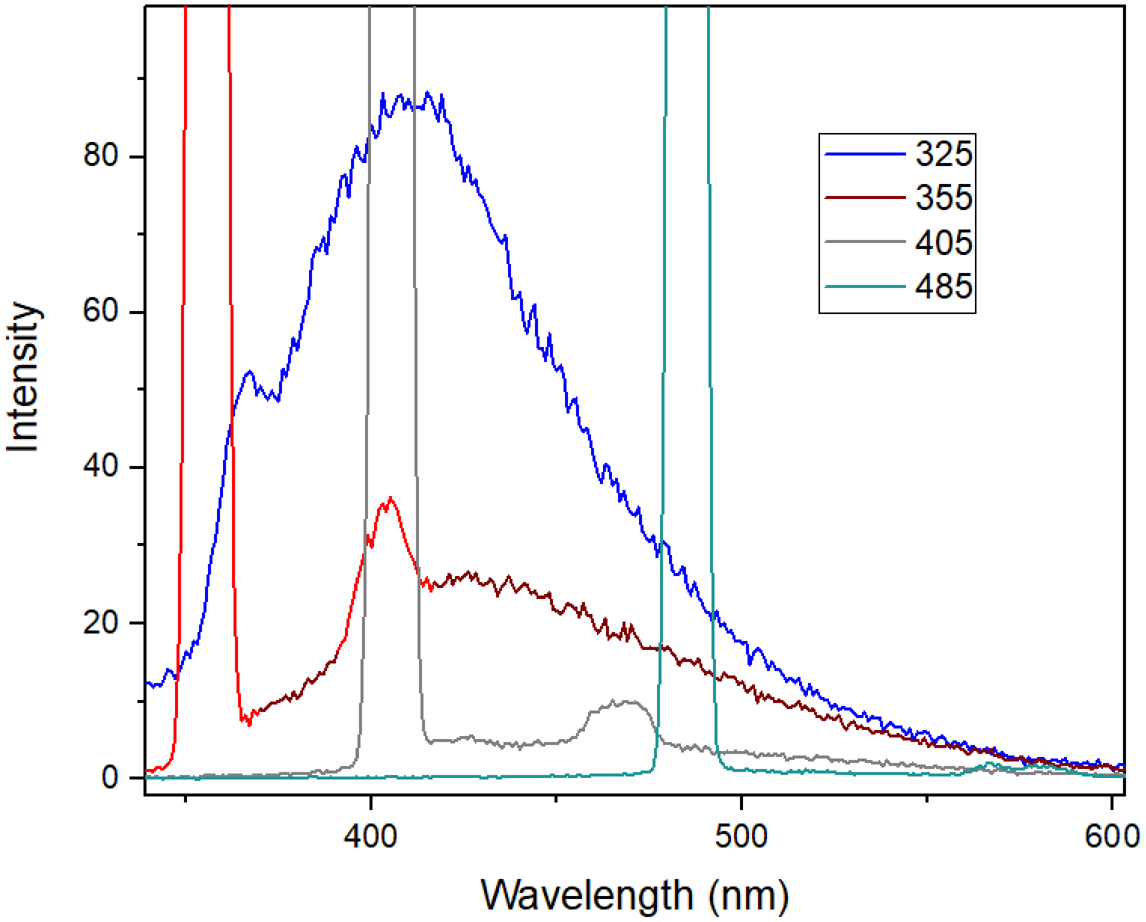

Figure S 4 ***Cary Agilent Spectrofluorometer data*** *showing emissions spectra for trimethyladamantylammonium hydroxide at 325, 355, 405, and 485 nm excitation*

Spectrofluorometer data shows the fluorescence emission response of the templating agent trimethyladamantylammonium hydroxide at selected wavelengths. At near-UV wavelengths like 325 nm, a clear fluorescence peak is seen at around 400 nm. With increasingly lower energy wavelengths the fluorescence emission is shown to decrease with the response at imaging wavelengths of 405 and 485 nm (shown for 488 nm) being very low. It is expected that at 405 nm and 488 nm, therefore, that the OSDA will not be directly visible.

2.5 Lifetime Values

Table S1. ***Lifetime and amplitude values chabazite calcined at 550 °C*** *for overall decay and four selected spatial regions of interest. A_i is the amplitude of the exponential component with exponential decay τ_i. $A_i\tau_i$% is the fractional amplitude, calculated as $A_i\tau_i/(A_1\tau_1 + A_2\tau_2 + A_3\tau_3)$, used to evaluate the weight of an exponential component. τ_{wavg} denotes the weighted average of the lifetimes τ.*

	ROI	**A_1**	**A_2**	**A_3**	**τ_1**	**τ_2**	**τ_3**	**$A_1\tau_1$%**	**$A_2\tau_2$%**	**$A_3\tau_3$%**	**τ_{wavg}**
Upper Plane	1	0.22	0.00	0.78	10.27	6.85	3.42	0.46	0.00	0.54	6.57
	2	0.21	0.48	0.31	12.59	4.98	0.99	0.50	0.45	0.06	8.53
Inner Plane	2	0.22	0.00	0.78	10.92	7.28	3.64	0.46	0.00	0.54	6.97
	3	0.25	0.00	0.75	16.62	11.09	5.46	0.50	0.00	0.49	11.09
	4	0.21	0.07	0.73	15.08	10.05	5.02	0.42	0.09	0.49	9.69
	5	0.07	0.29	0.64	10.01	2.98	0.58	0.36	0.45	0.19	5.07

Table S2. ***Table of lifetimes and amplitudes for chabazite calcined at 630 °C*** *in Figure S3 for top plane and central plane both overall and in each region of interest. A_i is the amplitude of the exponential component with exponential decay τ_i. $A_i\tau_i$% is the fractional amplitude, calculated as $A_i\tau_i/(A_1\tau_1 + A_2\tau_2 + A_3\tau_3)$, used to evaluate the weight of an exponential component. τ_{wavg} denotes the weighted average of the lifetimes τ.*

	ROI	**A_1**	**A_2**	**A_3**	**τ_1**	**τ_2**	**τ_3**	**$A_1\tau_1$%**	**$A_2\tau_2$%**	**$A_3\tau_3$%**	**τ_{wavg}**
Upper Plane	1	0.95	0.00	0.05	0.40	3.37	2.98	0.71	0.00	0.29	1.14
	2	0.15	0.18	0.67	18.25	12.17	6.08	0.30	0.25	0.46	11.19
Inner Plane	3	0.20	0.05	0.75	11.40	7.80	2.66	0.49	0.08	0.43	7.35
	4	0.14	0.02	0.84	8.91	6.37	1.22	0.51	0.06	0.43	5.45

2.6 Additional Confocal & FLIM Images

Figure S5 shows a schematic diagram of how z-stack images were acquired, as well as the methodology for selecting regions of interest for spectral analysis.

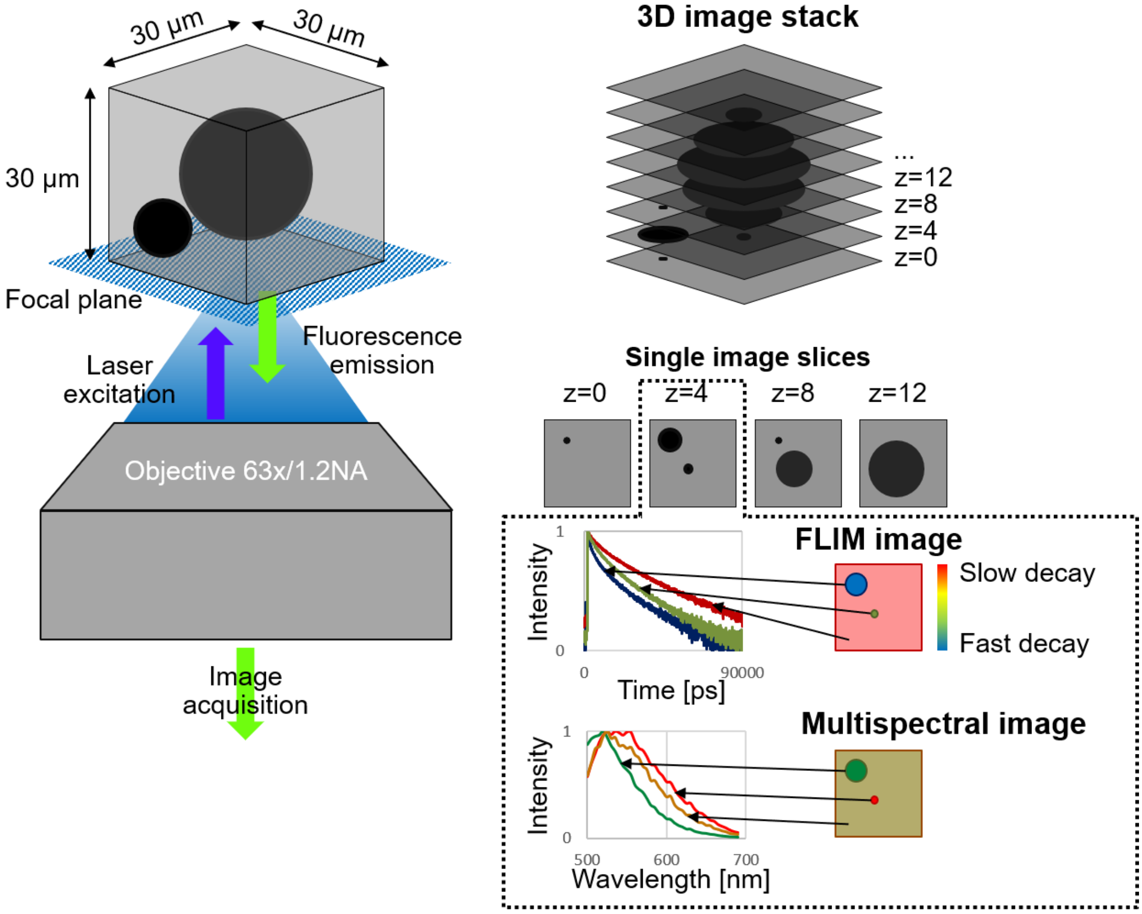

*Figure S 5 . **Scheme of principle of the Leica SP8 3D confocal acquisition**. In this microscopy technique, a sample is illuminated with a point scanning laser while the fluorescence is collected by an objective lens and sent to a detector to form an intensity-based image. A pinhole is placed in front of the detector to reject out-of-plane fluorescence and scattered light. By moving the sample through the focal plane, one can acquire a stack of images at varying sample depths in order to later reconstruct a 3D image. The same principle is used to acquire FLIM and multispectral images. In these cases, every pixel contains either decay information (FLIM image) or spectral information (multispectral image).*

Additional confocal z-stack slices and 3D constructions are presented here. Figure S6 shows further z-stack planes for two-colour confocal imaging. The ratio images have been calculate as channel in the longer wavelength range divided by the channel in the shorter wavelength range; the ratio shows in which areas the red emission is more pronounced compared to the shorter wavelength one.

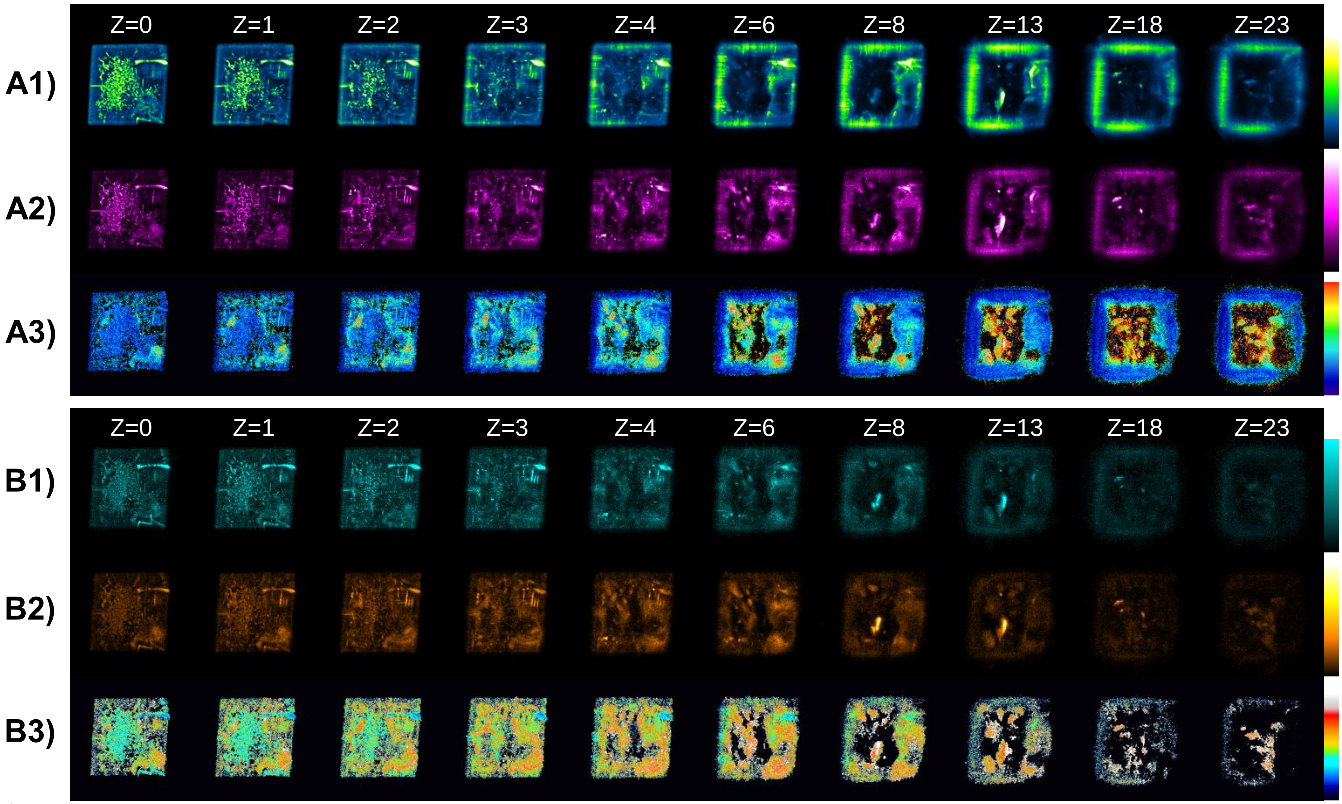

Figure S 6 . ***Selected z-stack planes for two-colour confocal images of chabazite calcined at 550 °C.*** ***A****) Single planes acquired under 405 nm laser excitation at different depths in the 450 to 550 nm emission channel (1), in the 580 to 700 nm emission channel (2) and the ratio image between the second and the first channel (3).* ***B****) Single planes acquired under 488 nm laser excitation at different depths in the 500 to 550 nm emission channel (1), in the 580 to 700 nm emission channel (2) and the ratio image between the second and the first channel (3).*

Figure S7 shows 3D reconstructions of confocal and FLIM z-stacks for chabazite calcined at 630 °C. Compared to chabazite calcined at 550 °C, the 630 °C has less emission across the crystal faces. As a result, in the 3D renders the internal occlusions are more visible. A concentration of emissive regions is seen localised clearly in the centre of the crystal. Figure S8 shows selected planes from the z-stack.

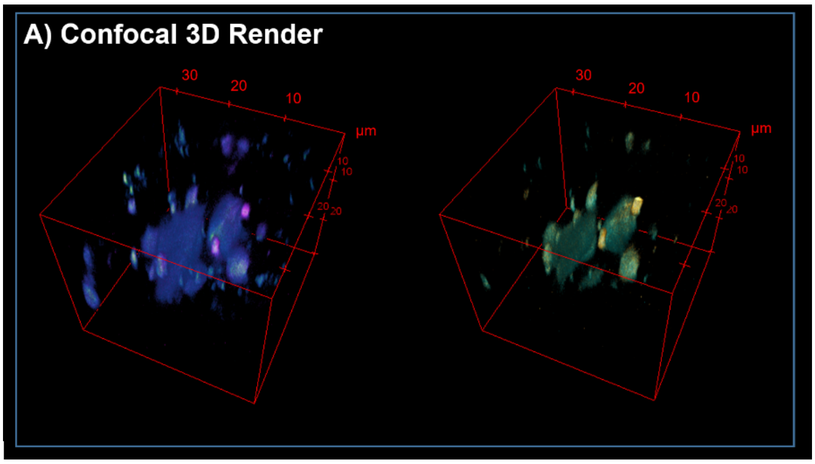

Figure S 7 ***3D reconstructions for chabazite calcined at 630 °C*** *obtained from a 2-colour stack of 120 slices acquired every 0.35 um at A)* λ_{ex}*=405 nm where the blue-green channel captures emission from 450-550 nm and is merged with the magenta channel capturing emission from 580-700 nm; B)* λ_{ex}*=488 nm where the cyan channel captures emission from 500-550 nm and is merged with the orange channel capturing emission from 580-700 nm.*

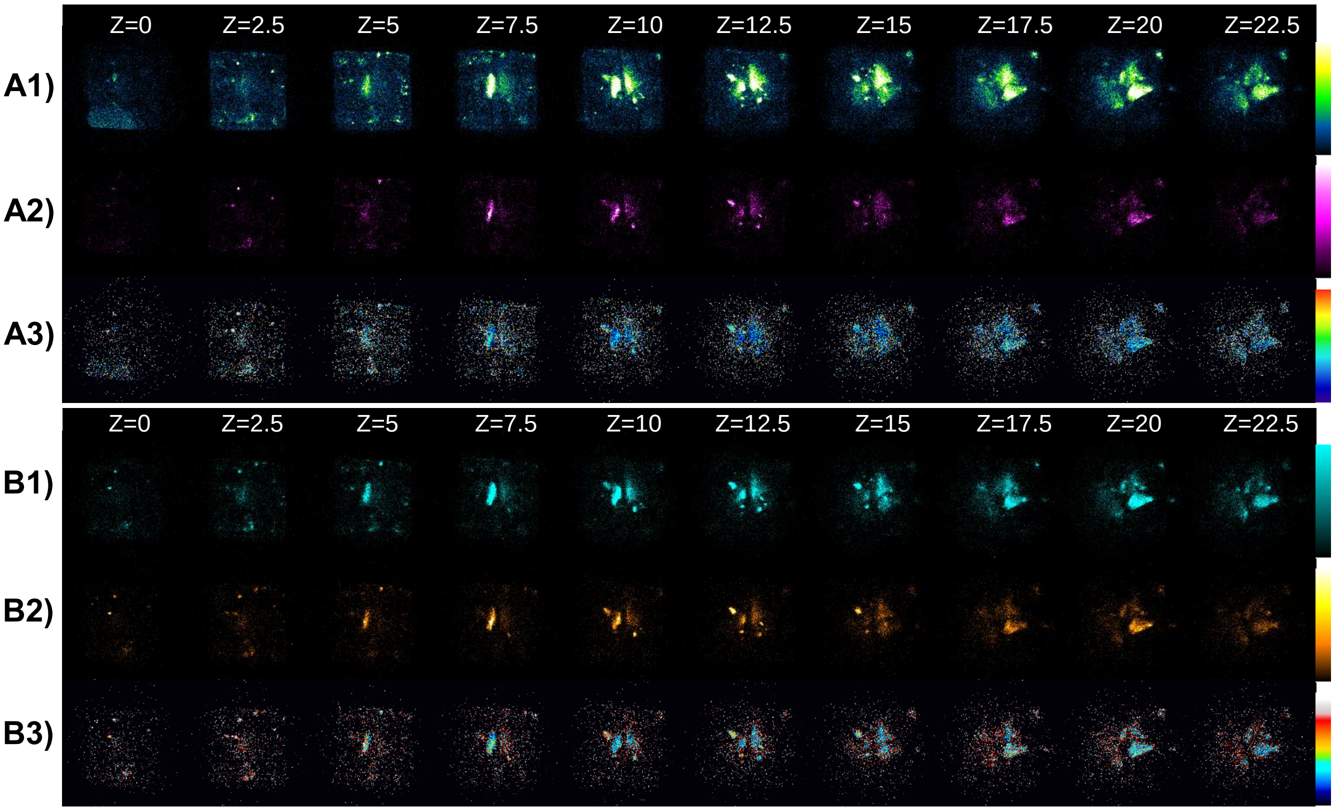

Figure S 8 ***Selected z-stack planes for two-colour confocal images of chabazite calcined at 630 °C. A)*** *Single planes acquired under 405 nm laser excitation at different depths in the 450 to 550 nm emission channel (1), in the 580 to 700 nm emission channel (2) and the ratio image between the second and the first channel (3).* ***B)*** *Single planes acquired under 488 nm laser excitation at different depths in the 500 to 550 nm emission channel (1), in the 580 to 700 nm emission channel (2) and the ratio image between the second and the first channel (3).*

3 Schematic Diagram of Deposits

Figure S9 is a schematic representation of the types of emissive deposits seen in the two samples. Both samples show evidence of two types of subsurface deposits, one of which is smaller with significant emission intensity (2 or 5) and another which appears as larger regions (3 or 5). Seen only in the 550 °C sample are the distribution of smaller agglomerates (1) across the crystal faces that appear to be confined to the first few microns of the external surfaces. In 3D slices of inner planes these deposits can be seen as fringing around the edge of the crystal perimeter.

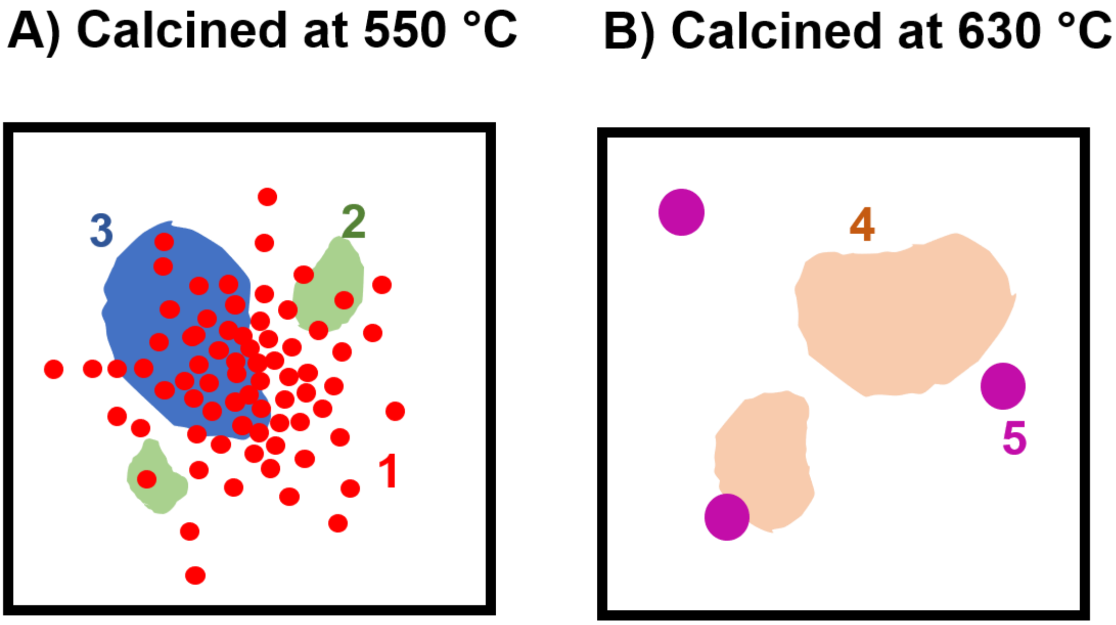

Figure S 9 ***Schematic diagram of different types of emissive deposits*** *discriminated on the basis of their shape and lifetime.*

4 References

[1] I. Lezcano-Gonzalez, U. Deka, B. Arstad, A. Van Yperen-De Deyne, K. Hemelsoet, M. Waroquier, V. Van Speybroeck, B. M. Weckhuysen, A. M. Beale, *Phys. Chem. Chem. Phys.* **2014**, *16*, 1639

[2] J. Schindelin, I. Arganda-Carreras, E. Frise, V. Kaynig, M. Longair, T. Pietzsch, S. Preibisch, C. Rueden, S. Saalfeld, B. Schmid, J.-Y. Tinevez, D. J. White, V. Hartenstein, K. Eliceiri, P. Tomancak, A. Cardona, *Nat. Methods* **2012**, *9*, 676–682.

[3] S. C. Warren, A. Margineanu, D. Alibhai, D. J. Kelly, C. Talbot, Y. Alexandrov, I. Munro, M. Katan, C. Dunsby, P. M. W. French, *PLoS One* **2013**, *8*, DOI 10.1371/journal.pone.0070687.

[4] M. A. Digman, V. R. Caiolfa, M. Zamai, E. Gratton, *Biophys. J.* **2008**, *94*, 14–16.

[5] J. Ofner, K. Kamilli, E. Eitenberger, G. Friedbacher, B. Lendl, A. Held, H. Lohninger, *Anal. Chem.* **2015**, 9413.

[6] S. Mosca, A. Artesani, D. Gulotta, A. Nevin, S. Goidanich, G. Valentini, D. Comelli, *Microchem. J.* **2018**, *139*, 500–505.

[7] H. Lohninger, J. Ofner, *Spectrosc. Eur.* **2014**, *26*, 6–10.

[8] C. J. Fahrni, *Curr. Opin. Chem. Biol.* **2007**, *11*, 121–127.

[9] S. Vogt, J. Maser, C. Jacobsen, *J. Phys. IV Fr.* **2003**, *104*, 617–622.

[10] Y. P. Hong, S. Chen, C. Jacobsen, *Proc. SPIE--the Int. Soc. Opt. Eng.* **2015**, *9592*, 95920W.

[11] C. Baerlocher, L. McCusker, “Database of Zeolite Structures,” can be found under http://www.iza-structure.org/databases/, **n.d.**

Please email Andrew.beale@ucl.ac.uk for copies of the raw data which includes: Raman, FLIM and XRF spectra.